https://doi.org/10.1016/j.jallcom.2021.160006

In-situ formation of bismuth nanoparticles on nickel foam for ambient ammonia synthesis via electrocatalytic nitrogen reduction

Guangzhe Li, Zhefei Pan, He Lin, Liang An*

Department of Mechanical Engineering, The Hong Kong Polytechnic University, Hung Hom, Kowloon, Hong Kong SAR, China

*Corresponding author.

Email: liang.an@polyu.edu.hk (L. An)

Abstract

Bismuth has been regarded as a promising electrocatalyst for triggering nitrogen reduction to ammonia, due to the ease of nitrogen dissociation rendered by the strong interaction between Bi 6p band and the N 2p orbitals. However, the poor conductivity of bismuth limits the electron transfer for nitrogen reduction. In addition, the sluggish water dissociation on the bismuth surface leads to insufficient proton supply for the protonation step of $*N_2$, causing inferior ammonia production performance. In this work, we prepare an integrated and binder-free bismuth nanoparticles@nickel foam electrode for ambient ammonia synthesis via a facile displacement reaction. Using nickel foam as the conductive substrate improves the electron transfer of bismuth for nitrogen reduction to ammonia. In addition, enhanced water dissociation on the nickel surface improves the protonation of $*N_2$ by supplying adequate protons via hydrogen spillover, thus boosting the ammonia production performance. This integrated electrode eliminates the use of polymer binders and reduces the contact resistance between the diffusion layer and catalyst layer, facilitating electron delivery and reducing cell

resistance, thus requiring less energy input for ammonia production. The performance examination in an electrochemical H-type cell shows that an ammonia yield rate as high as of 9.3×10^{-11} mol s^{-1} cm^{-2} and a Faradaic efficiency of 6.3 % are achieved. An ammonia yield rate of 8.19×10^{-11} mol s^{-1} cm^{-2} is observed after 6 cycles, with a retention rate of 88 %.

Keywords: Ambient ammonia synthesis; Electrocatalytic nitrogen reduction; Bismuth nanoparticles; Nickle foam; In-situ formation; Binder-free electrode

1. Introduction

Ammonia is not only a key industrial raw material to produce fertilizers, textiles and drugs [1,2], but also a promising energy carrier due to its high theoretical energy density (3 kW h kg^{-1}) and hydrogen content (17.7 wt. %) [3]. Ammonia, with a global output of around 150 million tons annually, is primarily produced by the Haber-Bosch process, which converts N_2 and H_2 to ammonia by using a metal catalyst at high temperatures (400 - 500 ^oC) and pressures (20 - 30 MPa) [4–7]. This process is highly energy intensive, consuming over 1 % global fossil fuels to reach such harsh reaction condition, and thus leading to 1.6 % CO_2 emission per year. In response to energy and environmental consequences, an alternative approach to produce ammonia, i.e., electrochemical ammonia synthesis [8–10], has been recently developed, capable of converting atmospheric nitrogen and water to ammonia and oxygen ($N_2 + 3H_2O \rightarrow 2NH_3 + 3/2O_2$) under ambient condition. The electrochemical synthesis method can be driven by intermittent energy such as wind and solar [11], thus contributing to energy and environmental sustainability.

The first step for realizing electrochemical nitrogen reduction to ammonia is the dissociation of nitrogen molecules. However, nitrogen is a stubbornly stable molecule with strong and nonpolarizable triple bonds, which requires a large overpotential to activate. Hence, an efficient electrocatalyst is highly desired to reduce the energy barrier for nitrogen dissociation. Until now, noble metal-based electrocatalysts [12], such as Au [13–15] and Ru [16–18], are reported as promising electrocatalysts for ammonia production. However, their scarcity and high cost hinder their industrialization for large-scale ammonia production. Alternatively, some non-noble metal-based electrocatalysts, such as Ni-based materials [19,20], can also be used for ammonia production. However, Ni-based materials often suffer from sluggish nitrogen

dissociation due to their low N binding energy for nitrogen activation ($* + N_2 \rightarrow *N_2$), thus lowering the ammonia production rate. Recently, bismuth is reported as a promising electrocatalyst for ammonia production [21,22], due to the strong interaction between the Bi 6p and the N 2p orbitals for nitrogen activation. However, using single bismuth electrocatalyst leads to sluggish water dissociation ($H_2O \rightarrow H^+ + OH^-$) [23], providing insufficient protons for the protonation of nitrogen ($*N_2 + 8H^+ + 6e^- \rightarrow * + 2NH_4^+$), thus lowering ammonia production rate. In addition, bismuth possesses poor electrical conductivity (1.25×10^6 S/m), which inhibits the electron transfer for nitrogen reduction [24].

Herein, we prepare an integrated and binder-free bismuth nanoparticles@nickel foam (BiNPs@NF) electrode for ambient ammonia synthesis via a facile displacement reaction. The fabrication of BiNPs@NF improves the poor conductivity of bismuth, due to the high conductivity of nickel (1.43×10^7 S/m). In addition, the higher electronegativity of bismuth (2.02) over nickel (1.91) also leads to accumulation of electrons at the side of bismuth, thus improving the intrinsic activity of bismuth electrocatalysts [25]. Moreover, strong dissociation of water on nickel surface [26] will generate a great amount of protons [27] at a high frequency, which will be transferred to adjacent bismuth surface by a spillover effect [28] via diffusion. The supply of protons can facilitate the nitrogen dissociation on the bismuth surface by protonation of $*N_2$, forming NH_3 ($*N_2 + 8H^+ + 6e^- \rightarrow * + 2NH_4^+$). In addition, the fabrication of BiNPs@NF electrode eliminates the use of polymer binders, which would create a barrier for electron delivery. Compared to the conventional electrode containing a diffusion layer and a catalyst layer and thus causing a large contact resistance between two layers [29], this integrated electrode reduces the contact resistance, thus requiring less energy input for ammonia production. By performance evaluation in a H-type cell,

an ammonia yield rate of 9.3×10^{-11} mol s^{-1} cm^{-2} is achieved and a high Faradaic efficiency of 6.3 % is observed. In addition, an ammonia yield rate of 8.19×10^{-11} mol s^{-1} cm^{-2} is found after 6 cycles with a retention rate of 88 %.

2. Experimental sections

2.1 Pretreatment and preparation

BiNPs@NF was prepared via a simple displacement reaction. A strip of nickel foam (1.0×2.0 cm^2) was first washed by DI water and ethanol for several times. To remove the oxide layer of nickel foam, it was annealed in the mixture gas of H_2 (5.0 vol. %) and Ar (95.0 vol. %) for 2 h at 800 ^oC. Next, it was immersed in the anhydrous glycol containing 0.1 mM $Bi(NO_3)_3 \cdot 5H_2O$ in a glove box filled with Ar gas. For the preparation of BiNPs, the nickel foam was kept in anhydrous glycol at room temperature for 18 h. For the preparation of bismuth nanoclusters (BiNCs), the nickel foam was kept in anhydrous glycol solution at 40 ^oC for 18 h. For the preparation of bismuth microplates (BiMPs), it was kept in anhydrous glycol solution at an elevated temperature of 80 ^oC for 18 h. After displacement reaction, the BiNPs@NF was taken out and washed by DI water and ethanol again. Subsequently, the BiNPs@NF was kept in the glove box filled with Ar gas to avoid surface oxidation of Bi. It was found that the surface of BiNPs will be oxidized and become Bi_2O_3 if it was kept in air for 2 - 3 days. For the pretreatment of Nafion membrane, it was boiled in 1.0 M NaOH solution for 2 h and subsequently boiled in DI water for 2 h.

2.2 Characterizations

The phase analysis of BiNPs@NF was conducted by X-ray diffraction (XRD) (D/max 2500PC) and the element analysis was conducted by energy-dispersive X-ray (EDX). The surface morphology of BiNPs@NF was observed by scanning electron microscopy (SEM) (Tescan MAIA3, Japan). The valence states of elements were analyzed by X-

ray photoelectron spectroscopy (XPS), recorded by a spectrometer with Mg/Al Kα radiation (Thermo VG Scientific, USA). As for the detection of ammonia ions in the test solution, the absorbance peak was measured by Ultraviolet (UV) adsorption spectra using UV-Vis double beam spectrophotometer (DB-20, Australia).

2.3 Electrochemical measurements

A three-electrode electrochemical system was constructed for the examination of nitrogen reduction reaction (NRR) properties of electrocatalysts. Typically, BiNPs@NF (1.0×2.0 cm^2) was used as the working electrode, commercial graphite plate (Hebei thermal insulation engineering Co., Ltd) with a geometric surface area of 2.0 cm^2 was used as the counter electrode and Hg/Hg_2SO_4 (MSE) was used as the reference electrode. The mass loading of BiNPs@NF was around 1.28 mg cm^{-2}. All the potentials were converted to reversible hydrogen electrode (RHE) [30]:

$$E_{RHE} = E_{MSE} + 0.059\ pH + 0.616 \quad (1)$$

0.5 M K_2SO_4 solution was used as the electrolyte and Nafion 115 membrane was also employed to separate cathode and anode compartments and transport ions during cell operation. The volume of electrolyte in each chamber was 100.0 mL. The cathodic reaction is the NRR[31]:

$$N_2 + 8H^+ + 6e^- \rightarrow 2NH_4^+ \qquad E^c = -0.078\ pH + 0.274\ V\ vs.\ RHE \quad (2)$$

The anodic reaction is the oxygen evolution reaction [32]:

$$3H_2O \rightarrow 6H^+ + 6e^- + O_2 \qquad E^a = 1.23\ V\ vs.\ RHE \quad (3)$$

Therefore, the overall reaction in neutral aqueous media can be expressed:

$$N_2 + 2H^+ + 3H_2O \rightarrow 2NH_4^+ + 3/2O_2 \qquad E^o = 0.956 + 0.019\ pH \quad (4)$$

At the inlet of cathode compartment, an acid trap containing 0.05 M H_2SO_4 was used to remove the ammonia contamination from the nitrogen source. In addition, an alkaline trap containing 0.05 M NaOH was used to remove the NO_x contamination from the

nitrogen source. At the outlet, an acid trap containing 0.05 M H_2SO_4 and a liquid seal was used to avoid the contamination from the air. All electrochemical measurements were carried out using Multi-Autolab electrochemical workstation (M204, Switzerland). Before cell operation, N_2 gas was bubbled into the cathode compartment for 1 h to exhaust the residual air in the chamber. A gas flowmeter was used to keep the gas flow rate at 20 mL min^{-1} during cell operation. In addition, a magnetic stirrer was used with a stirring rate of 200 r min^{-1} to help dissolution and even dispersion of N_2 gas. For the cyclic test, the electrocatalytic electrode previously used was repeatedly washed with DI water and then dried. The comparison test using Ar gas followed the same procedure as the N_2 test.

2.4 Detection and quantification of ammonia and hydrazine

The detection and quantification of ammonia ions were achieved by indophenol blue method [33]. First, chromogenic reagent was prepared by dissolving sodium citrate (3.0 wt. %) and salicylic acid (3.0 wt. %) in 1.0 M NaOH solution. For the color rendering of the test solution, 1.0 mL chromogenic solution was mixed with 0.5 mL sodium hypochlorite solution (5.0 wt. %) and 0.1 mL sodium nitroferricyanide dihydrate (1.0 wt. %), followed by adding 1.0 mL test solution. After 2 h, the mixed solution was transferred to a cuvette for the adsorption test, by measuring the adsorption peak intensity at 651 nm. For the measurement of standard adsorption curves of ammonia solution with known concentrations, a series of NH_4Cl solutions with different concentrations (0.0625, 0.125, 0.25, 0.5, 1.0 and 2.0 mg L^{-1}) containing 0.5 M K_2SO_4 were first prepared. Then, 1.0 mL standard NH_4Cl solution was mixed with the coloring reagent following the same procedure as the measurement of the test solution. Resultantly, the correlation between absorbance and ammonia concentration was established ($y = 0.25954\ x - 0.00584$) and a good linear fit ($R^2 = 0.9996$) was observed.

The detection of hydrazine in the test solution was achieved via the Watt and Chrisp method [34]. First, the color reagent was prepared by dissolving 0.199 g $C_9H_{11}NO$ into a mixture of 1.0 mL concentrated HCl (38 wt. %) and 10.0 mL absolute ethanol. Then, 1.0 mL color reagent was mixed with 1.0 mL test solution for color rendering. After 20 min, it was transferred to UV-vis double beam spectrophotometer, and the intensity of the absorption peak was measured at 457 nm. For the measurement of standard adsorption curves of hydrazine solution with known concentrations, a series of hydrazine solutions with different concentrations (0.15625, 0.3125, 0.625, 1.25 and 2.5 mg L^{-1}) containing 0.5 M K_2SO_4 were first prepared, followed by mixing with color reagents for adsorption tests. As a result, a relation between hydrazine concentration and absorbance was established ($y = 0.05588 + 0.96238\ x$) with a good linear fit ($R^2 = 0.9996$).

3. Results and discussion

The formation of bismuth on nickel via displacement reaction is thermodynamically feasible, as shown in Figure 1a, according to:

$$2Bi^{3+} + 3Ni \rightarrow 3Ni^{2+} + 2Bi \qquad \Delta G^{\theta} = -17.94\ kJ\ mol^{-1} \qquad (5)$$

Therefore, we attempt to prepare BiNPs@NF by immersing nickel foam into the anhydrous ethylene glycol containing 0.1 mM $Bi(NO_3)_3$. BiNPs@NF can be prepared by immersing nickel foam in the ethylene glycol solution for 18 h at room temperature, as revealed by the XRD pattern (Figure 1b). Three characteristic diffraction peaks at 27.16^o, 37.95^o and 39.62^o are indexed to the (012), (104) and (110) planes of bismuth (JCPDS no. 44-1246), respectively [35]. XPS spectra shows that the concentration (wt. %) of Bi and Ni on the surface of BiNPs@NF electrode is 64.59 % and 35.41 %, respectively, containing no other impurities. The valence state of Bi^0 is confirmed by observing two separated peaks centered at 157.08 eV and 162.48 eV, which can be

identified as Bi $4f_{7/2}$ and Bi $4f_{5/2}$ signals of Bi^0 [35], respectively, as shown in Figure 1c. In addition, Ni *2p* peaks centered at 855.68 eV and 873.18 eV are also observed (Figure 1d), corresponding to Ni$2p_{3/2}$ and Ni$2p_{1/2}$, respectively. We found that bismuth is deposited on the nickel foam surface without forming the Bi/Ni alloy, as revealed by XPS spectra (Figure 1d). The peak of Ni 2p will be shifted to a higher binding energy if Bi/Ni alloy forms [25]. However, the as-prepared bismuth nanoparticles@nickel foam displays no peak shift of Ni 2p, as compared to original nickel foam. BiNPs are evenly distributed on the entire nickel foam skeleton (Figures 2a-b), with an average particle size of 60 nm, as shown in the inset figure of Figure 2a. The successful growth and even distribution of BiNPs are further demonstrated by elemental mapping (Figures 2c-e) and EDX pattern (Figure 2f). We also found that by elevating the reaction temperature, the surface morphologies of bismuth can be significantly changed. Elevating the temperature to 40 ^oC leads to the formation of BiNCs, with a thickness of around 100 nm, as shown in Figure S1. Such a significant change can be attributed to the accelerated reaction kinetics at an elevated temperature. When further elevating the temperature to 80 ^oC, BiMPs are formed and these microplates are stacked upwards, protruding away from the nickel skeleton surface (Figure S2). The size of each plate is around tens of micrometers and the thickness of each plate is about 2 micrometers. The EDX pattern (Figure S3) of BiMPs shows distinct Bi signals due to their large particle size, in sharp contrast to that of BiNPs with weak Bi signals (Figure 2f).

NRR active sites are the three-phase reaction interface, including nitrogen (gas), protons (liquid) and electrons (solid). Their role is capable of simultaneously accepting nitrogen, protons and electrons for electrochemical nitrogen reduction ($N_2 + 8H^+ + 6e^- \rightarrow 2NH_4^+$). The NRR properties of BiNPs@NF are investigated using a setup containing acid trap, gas flowmeter, magnetic stirrer and a three-electrode

electrochemical cell (Figure S4). The voltage window for NRR is examined by linear sweep voltammetry (LSV) tests operating under different conditions of fed gases (N_2 or Ar). When using bare nickel foam as the working electrode (Figure 3a), there is no current difference under different conditions of fed gases, showing that bare nickel foam cannot be used for nitrogen reduction. The onset potential for electrochemical reaction is -0.18 V (vs. RHE), which is attributed to the hydrogen evolution reaction (HER) [36–38]. However, when using BiNPs@NF as the working electrode, the onset potential is negatively shifted to -0.27 V. The possible reason for this is that BiNPs can suppress the hydrogen evolution [39], since the current density for HER is significantly reduced by around 50 % (Figure 3b). A current gap is observed when using BiNPs@NF as working electrode with different fed gases (Figure 3a). Since Ar is a highly inert gas which cannot be electrochemically reduced, the additional current can only be contributed by the reduction of N_2 gas, thus revealing a voltage window for NRR from -0.375 V to -0.65 V. The current density for NRR (j_{NRR}) can be obtained by calculating the current difference of LSV curves, as shown in Figure 3c. A maximum j_{NRR} is observed at -0.525 V, and the decreased j_{NRR} observed at a more negative potential is because of the enhanced HER [40]. The Faradaic efficiency (FE) for NRR can also be obtained by the following equation [22]:

$$FE_{NRR}\ (\%) = (j_{N_2} - j_{Ar})/j_{N_2} \quad (6)$$

A maximum FE of 6.8 % for NRR is observed at -0.475 V, as shown in Figure 3d. The NRR properties of BiNCs and BiMPs electrocatalysts are also investigated by LSV tests (Figure S5 and S6). Similarly, the appearance of current gap also demonstrates the capability of NRR when using BiNCs@NF and BiMPs@NF as the working electrode. It is found that BiNPs@NF offers the best NRR property among three electrodes

(Figure S7), indicating that the size of electrocatalysts plays a decisive role in the NRR property. A smaller size of bismuth crystals can expose more active sites for NRR.

Theoretically, there are two possible products of electrochemical NRR, i.e., ammonia ions and hydrazine [31]. From a thermodynamics perspective, it is possible to generate both kinds of products when operating the cell at a potential below -0.332 V (vs. RHE), according to the Equation 2 and Equation 7 [31]:

$$N_2 + 4H_2O + 4e^- \rightarrow N_2H_4 + 4OH^- \quad E^o = -0.332 \text{ V vs. RHE} \tag{7}$$

For the examination of ammonia and hydrazine production, cell is operated at different potentials from -0.4 V to -0.6 V for 2 h (Figure 4a). The solution in cathode chamber is collected after cell operation and mixed with color reagent for UV-vis adsorption. As for the detection of ammonia ions, a highest adsorption peak is observed at -0.5 V centered at 652 nm, as shown in Figure 4b, indicating the maximum amount of ammonia production is achieved at -0.5 V. In comparison, no adsorption peak is observed under Ar condition (Figure S8). This demonstrates that the ammonia production only results from the NRR, eliminating the possibility of ammonia contamination during cell operation. In addition, no adsorption peak appears when using nickel foam as working electrode (Figure S8), indicating there is no contribution from the nickel foam substrate for ammonia production. Moreover, when operating the cell under open-circuit condition for 2 h in Ar, there is no ammonia production, confirming the stability of working electrode (Figure S9). The ammonia concentration in the cathode chamber after cell operation can be determined by comparing with the standard UV adsorption curves (Figure S10). Hence, the ammonia yield rate can be obtained [41]:

$$r_{NH_3} = (n \times V)/(t \times A) \tag{8}$$

Where n is the ammonia concentration, V represents the volume of the electrolyte, t stands for the reaction time and A is the geometric area. The Faradaic efficiency for ammonia production can be calculated as follow [41]:

$$FE\ (\%) = (3F \times n \times V)/(M \times Q) \quad (9)$$

Where F is the Faraday constant, M represents the relative molecular mass of NH_3, and Q stands for the total consumed charge during cell operation. The ammonia production performance is summarized in Figure 4c, showing a maximum ammonia yield rate of 9.3×10^{-11} mol s^{-1} cm^{-2} (or 5.68 μg h^{-1} cm^{-2}) at -0.5 V (vs. RHE), which is comparable with recently reported electrocatalysts (Table S1). Simultaneously, a Faradaic efficiency of 6.3 % is observed. As for the cyclic test of BiNPs@NF electrode, a good ammonia yield rate retention of 88 % is observed after 6 cycles, showing that BiNPs@NF electrode can be reversibly used for ammonia production. The high ammonia production rate results from the synergistic effect between bismuth and nickel (Figure 5). Using single bismuth electrocatalyst leads to sluggish protonation step due to the insufficient proton supply caused by poor catalytic properties of water dissociation of bismuth [23], as shown in Figure 5a. Using single nickel electrocatalyst also results in poor ammonia production performance due to its incapability of nitrogen adsorption (Figure 5b). In comparison, using BiNPs@NF electrode facilitates the nitrogen adsorption and simultaneously improves the proton supply by hydrogen spillover effect on nickel foam [28], thus facilitating the nitrogen reduction to ammonia (Figure 5c). As for the hydrazine production, the solution in cathode chamber is collected and mixed with coloring reagent for the adsorption test. Resultantly, no adsorption peak appears when operating the cell at different potentials (Figure S11 and Figure S12), suggesting no hydrazine production during the NRR.

4. Concluding remarks

In summary, we prepare an integrated and binder-free bismuth nanoparticles@nickel foam electrode via a facile displacement reaction for efficient ammonia synthesis. The synergistic effect between bismuth and nickel facilitates nitrogen reduction to ammonia, in which bismuth acts as active sites for nitrogen adsorption ($* + N_2 \rightarrow *N_2$) and nickel with strong water dissociation can supply sufficient protons for protonation of $*N_2$ ($*N_2 + 8H^+ + 6e^- \rightarrow * + 2NH_4^+$). This integrated electrode also eliminates the use of binders and reduces the contact resistance between diffusion layer and catalyst layer, promoting the electron delivery for nitrogen reduction to ammonia. The performance examination in an electrochemical H-type cell displays a high ammonia yield rate of 9.3×10^{-11} mol s^{-1} cm^{-2} and a Faradaic efficiency of 6.3 %. This significant advance opens a window of opportunity for breakthroughs in the development of ambient ammonia synthesis technologies.

Conflicts of interest:

There are no conflicts to declare.

Acknowledgement:

Supports for this work from a grant from the Research Grants Council of the Hong Kong Special Administrative Region, China (Project No. 15222018) and a Central Research Grant from The Hong Kong Polytechnic University (PolyU 1-ZE30) are acknowledged.

References

[1] A.J. Medford, M.C. Hatzell, Photon-Driven Nitrogen Fixation: Current Progress, Thermodynamic Considerations, and Future Outlook, ACS Catal. 7 (2017) 2624–2643. doi:10.1021/acscatal.7b00439.

[2] Y. Zhao, R. Shi, X. Bian, C. Zhou, Y. Zhao, S. Zhang, F. Wu, G.I.N. Waterhouse, L.Z. Wu, C.H. Tung, T. Zhang, Ammonia Detection Methods in Photocatalytic and Electrocatalytic Experiments: How to Improve the Reliability of NH 3 Production Rates?, Adv. Sci. 6 (2019) 1802109. doi:10.1002/advs.201802109.

[3] Y. Guo, Z. Pan, L. An, Carbon-free sustainable energy technology: Direct ammonia fuel cells, J. Power Sources. 476 (2020) 228454. doi:10.1016/j.jpowsour.2020.228454.

[4] J. Deng, J.A. Iñiguez, C. Liu, Electrocatalytic Nitrogen Reduction at Low Temperature, Joule. 2 (2018) 846–856. doi:10.1016/j.joule.2018.04.014.

[5] M. Li, H. Huang, J. Low, C. Gao, R. Long, Y. Xiong, Recent Progress on Electrocatalyst and Photocatalyst Design for Nitrogen Reduction, Small Methods. 3 (2019) 1800388. doi:10.1002/smtd.201800388.

[6] R. Zhao, H. Xie, L. Chang, X. Zhang, X. Zhu, X. Tong, T. Wang, Y. Luo, P. Wei, Z. Wang, X. Sun, Recent progress in the electrochemical ammonia synthesis under ambient conditions, EnergyChem. 1 (2019) 100011. doi:10.1016/j.enchem.2019.100011.

[7] K.H. Liu, H.X. Zhong, S.J. Li, Y.X. Duan, M.M. Shi, X.B. Zhang, J.M. Yan, Q. Jiang, Advanced catalysts for sustainable hydrogen generation and storage via

hydrogen evolution and carbon dioxide/nitrogen reduction reactions, Prog. Mater. Sci. 92 (2018) 64–111. doi:10.1016/j.pmatsci.2017.09.001.

[8] S. Liu, M. Wang, T. Qian, H. Ji, J. Liu, C. Yan, Facilitating nitrogen accessibility to boron-rich covalent organic frameworks via electrochemical excitation for efficient nitrogen fixation, Nat. Commun. 10 (2019) 3898. doi:10.1038/s41467-019-11846-x.

[9] M. Wang, S. Liu, H. Ji, J. Liu, C. Yan, T. Qian, Unveiling the Essential Nature of Lewis Basicity in Thermodynamically and Dynamically Promoted Nitrogen Fixation, Adv. Funct. Mater. 30 (2020) 2001244. doi:https://doi.org/10.1002/adfm.202001244.

[10] G. Li, Y. Yu, Z. Pan, L. An, Two-dimensional layered SnO2 nanosheets for ambient ammonia synthesis, ACS Appl. Energy Mater. 3 (2020) 6735–6742. doi:10.1021/acsaem.0c00858.

[11] G. Li, B. Huang, Z. Pan, X. Su, Z. Shao, L. An, Advances in three-dimensional graphene-based materials: Configurations, preparation and application in secondary metal (Li, Na, K, Mg, Al)-ion batteries, Energy Environ. Sci. 12 (2019) 2030–2053. doi:10.1039/c8ee03014f.

[12] B.H.R. Suryanto, H.L. Du, D. Wang, J. Chen, A.N. Simonov, D.R. MacFarlane, Challenges and prospects in the catalysis of electroreduction of nitrogen to ammonia, Nat. Catal. 2 (2019) 290–296. doi:10.1038/s41929-019-0252-4.

[13] M.M. Shi, D. Bao, B.R. Wulan, Y.H. Li, Y.F. Zhang, J.M. Yan, Q. Jiang, Au Sub-Nanoclusters on TiO2 toward Highly Efficient and Selective Electrocatalyst

for N2 Conversion to NH3 at Ambient Conditions, Adv. Mater. 29 (2017) 2–7. doi:10.1002/adma.201606550.

[14] J. Zheng, Y. Lyu, M. Qiao, J.P. Veder, R.D. Marco, J. Bradley, R. Wang, Y. Li, A. Huang, S.P. Jiang, S. Wang, Tuning the Electron Localization of Gold Enables the Control of Nitrogen-to-Ammonia Fixation, Angew. Chemie - Int. Ed. 58 (2019) 18604–18609. doi:10.1002/anie.201909477.

[15] H. Wang, D. Yang, S. Liu, S. Yin, H. Yu, Y. Xu, X. Li, Z. Wang, L. Wang, Amorphous Sulfur Decorated Gold Nanowires as Efficient Electrocatalysts toward Ambient Ammonia Synthesis, ACS Sustain. Chem. Eng. (2019) 5–10. doi:10.1021/acssuschemeng.9b05542.

[16] S.Z. Andersen, V. Čolić, S. Yang, J.A. Schwalbe, A.C. Nielander, J.M. McEnaney, K. Enemark-Rasmussen, J.G. Baker, A.R. Singh, B.A. Rohr, M.J. Statt, S.J. Blair, S. Mezzavilla, J. Kibsgaard, P.C.K. Vesborg, M. Cargnello, S.F. Bent, T.F. Jaramillo, I.E.L. Stephens, J.K. Nørskov, I. Chorkendorff, A rigorous electrochemical ammonia synthesis protocol with quantitative isotope measurements, Nature. 570 (2019) 504–508. doi:10.1038/s41586-019-1260-x.

[17] S. Cheng, Y.-J. Gao, Y.-L. Yan, X. Gao, S.-H. Zhang, G.-L. Zhuang, S.-W. Deng, Z.-Z. Wei, X. Zhong, J.-G. Wang, Oxygen vacancy enhancing mechanism of nitrogen reduction reaction property in Ru/TiO2, J. Energy Chem. 39 (2019) 144–151. doi:https://doi.org/10.1016/j.jechem.2019.01.020.

[18] Y. Yao, H. Wang, X. Yuan, H. Li, M. Shao, Electrochemical Nitrogen Reduction Reaction on Ruthenium, ACS Energy Lett. 4 (2019) 1336–1341. doi:10.1021/acsenergylett.9b00699.

[19] Y. Chen, B. Wu, B. Sun, N. Wang, W. Hu, S. Komarneni, N-Doped Porous Carbon Self-Generated on Nickel Oxide Nanosheets for Electrocatalytic N2 Fixation with a Faradaic Efficiency beyond 30%, ACS Sustain. Chem. Eng. 7 (2019) 18874–18883. doi:10.1021/acssuschemeng.9b04024.

[20] K. Chu, Y.P. Liu, J. Wang, H. Zhang, NiO Nanodots on Graphene for Efficient Electrochemical N2 Reduction to NH3, ACS Appl. Energy Mater. 2 (2019) 2288–2295. doi:10.1021/acsaem.9b00102.

[21] L. Li, C. Tang, B. Xia, H. Jin, Y. Zheng, S.Z. Qiao, Two-Dimensional Mosaic Bismuth Nanosheets for Highly Selective Ambient Electrocatalytic Nitrogen Reduction, ACS Catal. 9 (2019) 2902–2908. doi:10.1021/acscatal.9b00366.

[22] Y.C. Hao, Y. Guo, L.W. Chen, M. Shu, X.Y. Wang, T.A. Bu, W.Y. Gao, N. Zhang, X. Su, X. Feng, J.W. Zhou, B. Wang, C.W. Hu, A.X. Yin, R. Si, Y.W. Zhang, C.H. Yan, Promoting nitrogen electroreduction to ammonia with bismuth nanocrystals and potassium cations in water, Nat. Catal. 2 (2019) 448–456. doi:10.1038/s41929-019-0241-7.

[23] R. Gómez, A. Fernández-Vega, J.M. Feliu, A. Aldaz, Effects of irreversibly adsorbed bismuth and antimony on hydrogen adsorption and evolution on Pt(100), J. Phys. Chem. 97 (1993) 4769–4776. doi:10.1021/j100120a032.

[24] D. Yao, C. Tang, L. Li, B. Xia, A. Vasileff, H. Jin, Y. Zhang, S.Z. Qiao, In Situ Fragmented Bismuth Nanoparticles for Electrocatalytic Nitrogen Reduction, Adv. Energy Mater. 10 (2020) 1–8. doi:10.1002/aenm.202001289.

[25] Z. Fang, P. Wu, Y. Qian, G. Yu, Gel-Derived Amorphous Bismuth–Nickel Alloy Promotes Electrocatalytic Nitrogen Fixation via Optimizing Nitrogen Adsorption and Activation, Angew. Chemie - Int. Ed. 60 (2020) 4275–4281. doi:10.1002/anie.202014302.

[26] N. Gerrard, K. Mistry, G.R. Darling, A. Hodgson, Water Dissociation and Hydroxyl Formation on Ni(110), J. Phys. Chem. C. 124 (2020) 23815–23822. doi:10.1021/acs.jpcc.0c08708.

[27] G. Chen, T. Wang, P. Liu, Z. Liao, H. Zhong, G. Wang, P. Zhang, M. Yu, E. Zschech, M. Chen, J. Zhang, X. Feng, Promoted oxygen reduction kinetics on nitrogen-doped hierarchically porous carbon by engineering proton-feeding centers, Energy Environ. Sci. 13 (2020) 2849–2855. doi:10.1039/d0ee01613f.

[28] W. Karim, C. Spreafico, A. Kleibert, J. Gobrecht, J. Vandevondele, Y. Ekinci, J.A. Van Bokhoven, Catalyst support effects on hydrogen spillover, Nature. 541 (2017) 68–71. doi:10.1038/nature20782.

[29] Y.S. Li, T.S. Zhao, A high-performance integrated electrode for anion-exchange membrane direct ethanol fuel cells, Int. J. Hydrogen Energy. 36 (2011) 7707–7713. doi:10.1016/j.ijhydene.2011.03.090.

[30] Y. Liu, D. Li, J. Yu, B. Ding, Stable Confinement of Black Phosphorus Quantum Dots on Black Tin Oxide Nanotubes: A Robust, Double-Active Electrocatalyst

toward Efficient Nitrogen Fixation, Angew. Chemie. 131 (2019) 16591–16596. doi:10.1002/ange.201908415.

[31] W. Guo, K. Zhang, Z. Liang, R. Zou, Q. Xu, Electrochemical nitrogen fixation and utilization: Theories, advanced catalyst materials and system design, Chem. Soc. Rev. 48 (2019) 5658–5716. doi:10.1039/c9cs00159j.

[32] C. Tang, H. Sen Wang, H.F. Wang, Q. Zhang, G.L. Tian, J.Q. Nie, F. Wei, Spatially Confined Hybridization of Nanometer-Sized NiFe Hydroxides into Nitrogen-Doped Graphene Frameworks Leading to Superior Oxygen Evolution Reactivity, Adv. Mater. 27 (2015) 4516–4522. doi:10.1002/adma.201501901.

[33] H.K. Lee, C.S.L. Koh, Y.H. Lee, C. Liu, I.Y. Phang, X. Han, C.-K.K. Tsung, X.Y. Ling, C. Liu, H.K. Lee, C.-K.K. Tsung, X.Y. Ling, I.Y. Phang, C.S.L. Koh, Y.H. Lee, Favoring the unfavored: Selective electrochemical nitrogen fixation using a reticular chemistry approach, Sci. Adv. 4 (2018) 1–8. doi:10.1126/sciadv.aar3208.

[34] H. COHEN, R.D. BARNARD, Spectrophotometric Method for Determination of Hydrazine, Anal. Chem. 24 (1952) 2006–2008. doi:10.1093/ajcp/16.7_ts.134.

[35] Y. Wang, M. miao Shi, D. Bao, F. lu Meng, Q. Zhang, Y. tong Zhou, K. hua Liu, Y. Zhang, J. zhi Wang, Z. wen Chen, D. peng Liu, Z. Jiang, M. Luo, L. Gu, Q. hua Zhang, X. zhong Cao, Y. Yao, M. hua Shao, Y. Zhang, X.B. Zhang, J.G. Chen, J. min Yan, Q. Jiang, Generating Defect-Rich Bismuth for Enhancing the Rate of Nitrogen Electroreduction to Ammonia, Angew. Chemie - Int. Ed. 58 (2019) 9464–9469. doi:10.1002/anie.201903969.

[36] Y. Huang, Y.E. Miao, J. Fu, S. Mo, C. Wei, T. Liu, Perpendicularly oriented few-layer MoSe2 on SnO2 nanotubes for efficient hydrogen evolution reaction, J. Mater. Chem. A. 3 (2015) 16263–16271. doi:10.1039/c5ta03704b.

[37] Y. Huang, Y.E. Miao, L. Zhang, W.W. Tjiu, J. Pan, T. Liu, Synthesis of few-layered MoS2 nanosheet-coated electrospun SnO2 nanotube heterostructures for enhanced hydrogen evolution reaction, Nanoscale. 6 (2014) 10673–10679. doi:10.1039/c4nr02014f.

[38] S. Ravula, C. Zhang, J.B. Essner, J.D. Robertson, J. Lin, G.A. Baker, Ionic Liquid-Assisted Synthesis of Nanoscale (MoS2)x(SnO2)1-x on Reduced Graphene Oxide for the Electrocatalytic Hydrogen Evolution Reaction, ACS Appl. Mater. Interfaces. 9 (2017) 8065–8074. doi:10.1021/acsami.6b13578.

[39] Y. Sun, Z. Deng, X.M. Song, H. Li, Z. Huang, Q. Zhao, D. Feng, W. Zhang, Z. Liu, T. Ma, Bismuth-Based Free-Standing Electrodes for Ambient-Condition Ammonia Production in Neutral Media, Nano-Micro Lett. 12 (2020) 133–145. doi:10.1007/s40820-020-00444-y.

[40] C. Choi, S. Back, N.Y. Kim, J. Lim, Y.H. Kim, Y. Jung, Suppression of Hydrogen Evolution Reaction in Electrochemical N2 Reduction Using Single-Atom Catalysts: A Computational Guideline, ACS Catal. 8 (2018) 7517–7525. doi:10.1021/acscatal.8b00905.

[41] G.-F. Chen, S. Ren, L. Zhang, H. Cheng, Y. Luo, K. Zhu, L.-X. Ding, H. Wang, Advances in Electrocatalytic N 2 Reduction-Strategies to Tackle the Selectivity Challenge , Small Methods. 3 (2019) 1800337. doi:10.1002/smtd.201800337.

Figures:

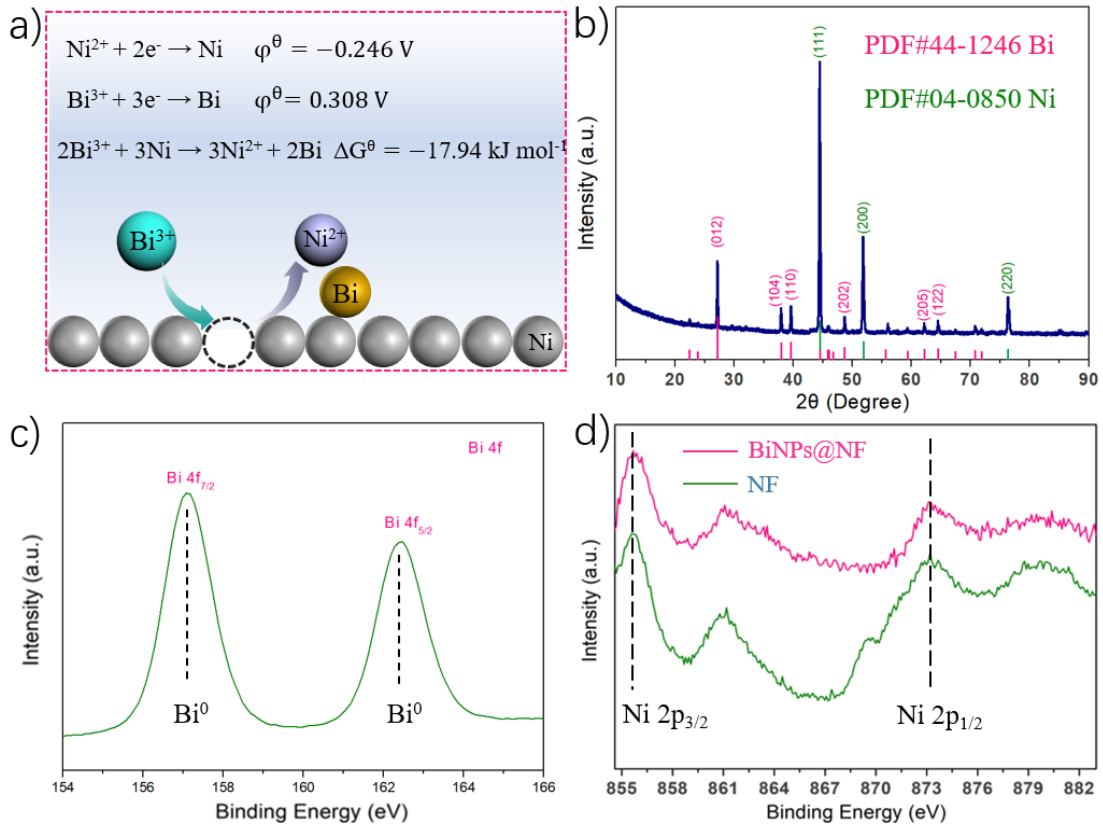

Figure 1 (a) Thermodynamic feasibility of in-situ formation of bismuth on nickel foam at room temperature. (b) XRD pattern showing the successful loading of bismuth on nickel foam. XPS spectra of (c) bismuth confirming the existence of Bi^0 and (d) Ni 2p peaks of BiNPs@NF electrode and bare nickel foam without electrocatalysts.

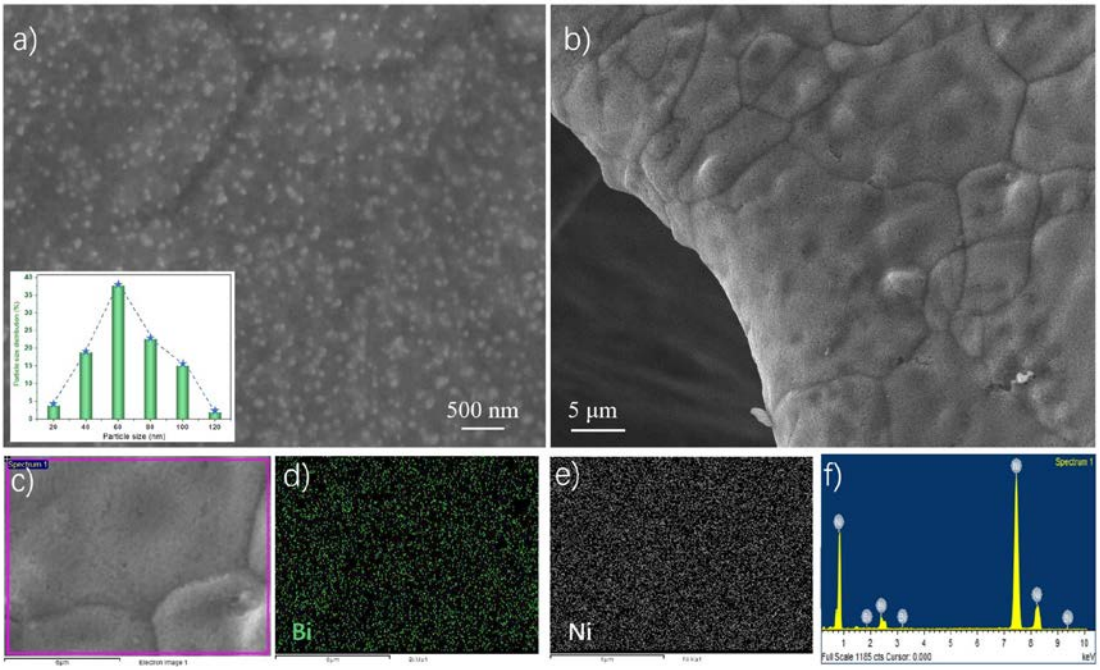

Figure 2 (a-b) Surface morphologies of BiNPs@NF and its phase analysis by (c-e) elemental mapping and (f) EDX pattern.

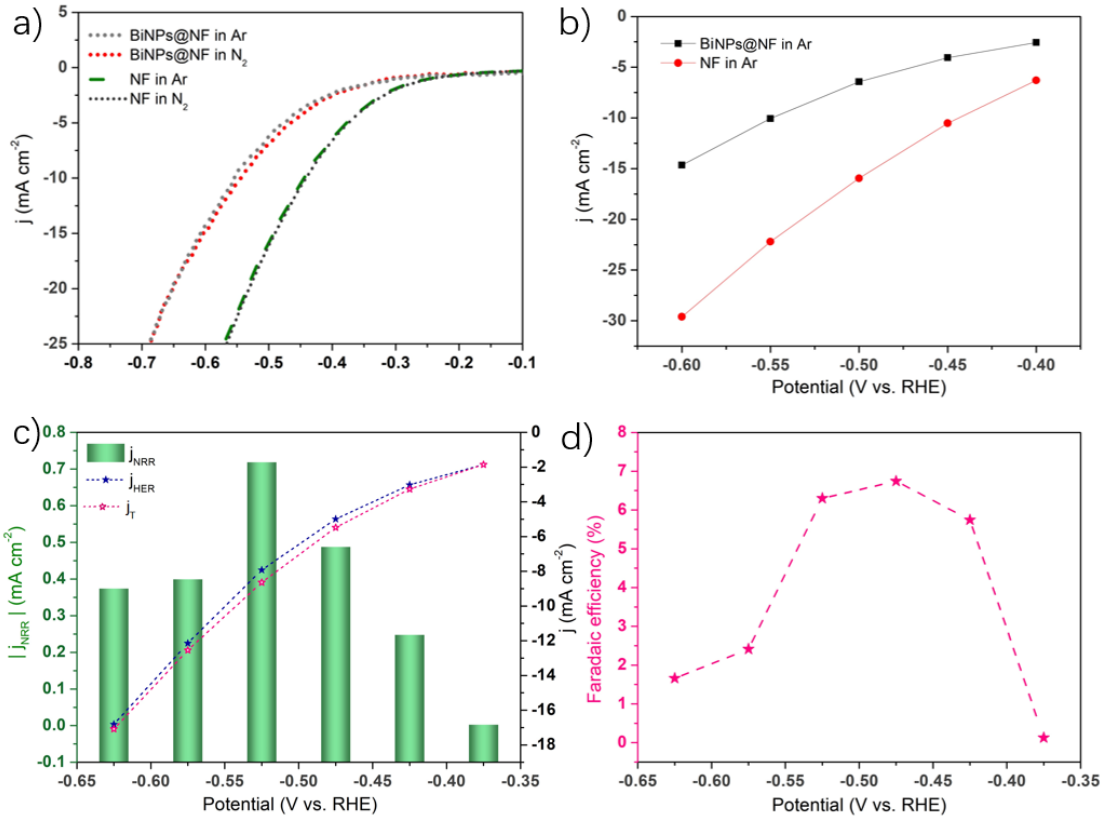

Figure 3 (a) LSV tests under various operating conditions. (b) HER comparison between BiNPs@NF and nickel foam. (c) Total current and current distribution for NRR and HER. (d) Faradaic efficiencies.

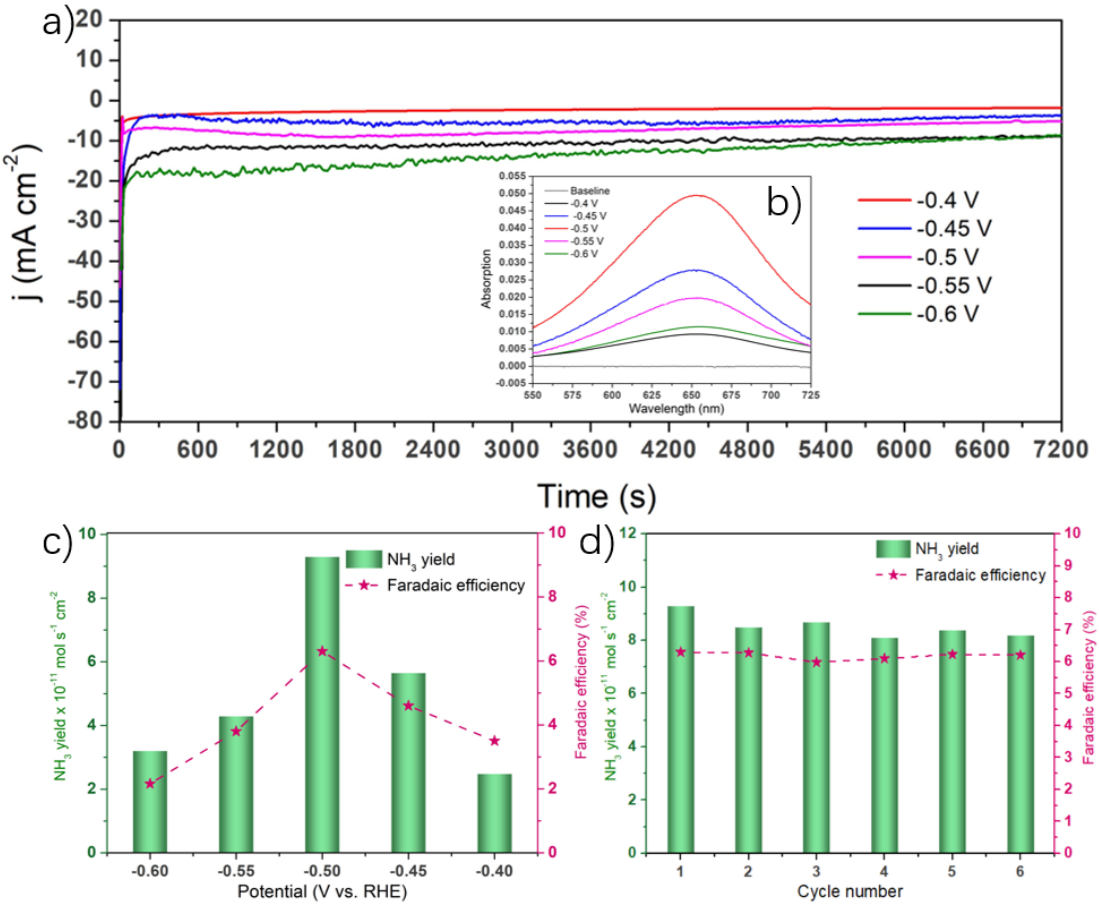

Figure 4 (a) Electrocatalytic NRR at different potentials. (b) UV adsorption spectra after 2-hour cell operation. (c) Ammonia production performance. (d) Cyclic stability.

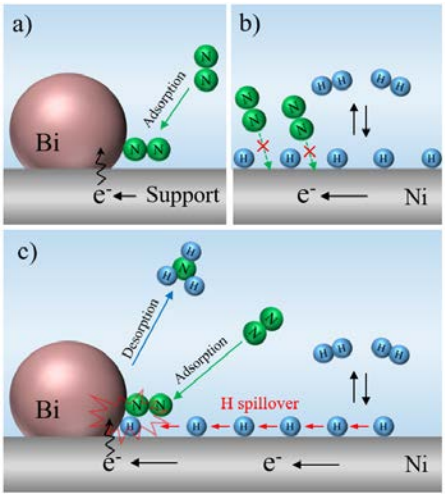

Figure 5 A comparison of catalytic properties of different electrodes. (a) The deposition of bismuth on inactive conductive support. (b) Nickel foam. (c) The deposition of bismuth nanoparticles on nickel foam.